SCIENTIFIC REPORTS
nature research

OPEN

Indeno[1,2-*b*]thiophene End-capped Perylene Diimide: Should the 1,6-Regioisomers be systematically considered as a byproduct?

Pablo Simón Marqués[1], Francesco Tintori[2], José María Andrés Castán[1], Pierre Josse[1], Clément Dalinot[1], Magali Allain[1], Gregory Welch[2*], Philippe Blanchard[1*] & Clément Cabanetos[1*]

Usually considered as a byproduct, the *1,6*-dibrominated PDI has rarely been functionalized for the preparation of electro-active conjugated molecules, particularly in the field of organic photovoltaics. In light of the literature, one can ask oneself: Does a *1,7*-isomer based functional molecule systematically perform better than its *1,6*-analogue? To answer this question, we report herein the synthesis and direct comparison of two indeno[1,2-*b*]thiophene (IDT) end-capped perylene diimide regioisomers (PDI) (*1,6* and *1,7*) used as non-fullerene acceptors in organic solar cells. It turned out that in our case, *ie*, when blended with the well-known PTB7-Th donor polymer, higher performance was reached for devices made with the *1,6*-analogue.

Major contributors to the recent resurgence of organic photovoltaics (OPVs)[1–3], molecular non-fullerene acceptors (NFAs) have driven up power conversion efficiencies (PCEs), in a short amount of time, from "what a fullerene derivative does best"[4,5] to more than 15%[6–8]. Although these records were reached with indacenodithiophene derivatives, perylene diimides (PDIs) have always held an important place among the electron transporting materials due to their excellent thermal, chemical and photochemical stabilities combined with their singular optical, redox and charge transport properties[9,10]. Nonetheless, the PDI extended π-conjugated structure typically suffers from an excessive π–π stacking tendency, forming micrometer-sized crystallites that are detrimental for an efficient charge separation in bulk heterojunction (BHJ) solar cells[11–14]. To tackle this problem, important efforts have been devoted to functionalize the peripheral positions, namely the bay (1,6,7,12) and *ortho* positions (2,5,8,11)[3,9,15–18], leading to profuse design principles and above all, to a better understanding of the structure-property relationships (Fig. 1)[19–28].

The key reaction, the dibromination of the bay positions, holds a special place by providing a precursor to many published molecular and macromolecular π-functional PDI based materials, namely the *1,7*-isomer[29]. Also generated during the reaction, but in smaller ratio, the *1,6*-isomer has not triggered such interest. Conversely, the latter has even motivated the development of purification procedures and methods since usually considered as an impurity[30].

As a result, only limited studies aiming at comparing the properties of molecular architectures based on both regioisomers have been reported so far[31–33], particularly in the field of OPVs. In fact, and to the best of our knowledge, only one paper can be found where the two bromo isomers (*1,6* and *1,7*) were functionalized either by triphenylamine (TPA) or benzodithiophene (BDT) moieties for the preparation of NFAs[34]. In all cases, best PCEs (*ca* 0.67%) were reached with the *1,7*-isomers once blended with different donor polymers and attributed to a better phase separation. Considering the scarcity of reported examples, it would be unthinkable to draw meaningful conclusions on the systematic use of one isomer over the other.

[1]CNRS UMR 6200, MOLTECH-Anjou, University of Angers, 2 Bd Lavoisier, 49045, Angers, France. [2]Department of Chemistry, University of Calgary, 2500 University Drive N.W., Calgary, Alberta, T2N 1N4, Canada. *email: gregory.welch@ucalgary.ca; philippe.blanchard@univ-angers.fr; clement.cabanetos@univ-angers.fr

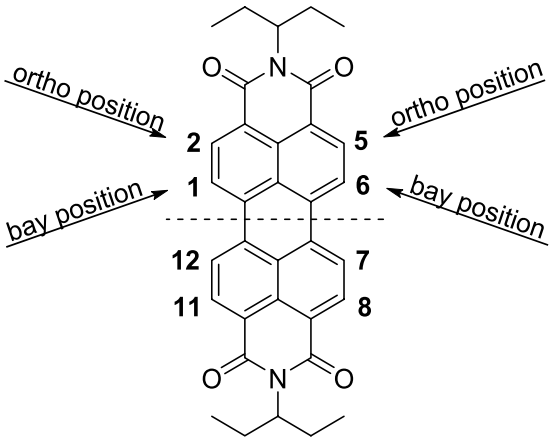

Figure 1. Molecular structure of the perylene diimide chromophore.

Consequently, to gain further insight into these differences, particularly from a charge transport point of view, the synthesis and direct comparison of two new indeno[1,2-*b*]thiophene (IDT) end-capped PDI regioisomers (*1,6* and *1,7*) is reported herein.

Results and Discussion

The synthetic route to both target regioisomers **1,7-i** and **1,6-i** is depicted in Scheme 1.

Stemming from the current high efficient NFAs[3,35,36], the bulky IDT derivative (**4**), used herein to restrain the PDI aggregation in **1,7-i** and **1,6-i**, was first prepared in three steps starting with a Stille pallado-catalysed reaction between the methyl 2-bromobenzoate **1** and the 2-tributylstannylthiophene to afford compound **2**. The latter was then treated with *p*-tolyllithium to generate a benzyl alcohol intermediate that was subsequently cyclized under acidic conditions. The resulting indeno[1,2-*b*]thiophene **3** was finally stannylated in presence of *n*-BuLi and trimethyltin chloride. In parallel, a 3:1 ratio mixture of *1,7* and *1,6* dibrominated PDIs was efficiently prepared following a method reported by Rybtchinski & *al.*[37] before being directly engaged in a final Stille cross-coupling reaction with the stannyl derivative **4** to afford the mixture of target isomers that were easily separated by column chromatography.

Analyzed by ^{1}H NMR spectroscopy, the latter exhibit similar sets of signals with only subtle changes, as depicted in Fig. 2. In fact, only the singlet signal associated to the proton born by the thiophene ring showed a significantly different chemical shift at 6.96 ppm and 7.17 pm for **1,6-i** and **1,7-i** respectively (pink circle, Fig. 2).

Although structural attribution can be deduced from the ^{13}C NMR spectra, and more precisely from the number of aliphatic carbon that are symmetry dependent (Fig. S11), single crystals of both isomers were grown by the solvent evaporation method. While slow evaporation from dichloromethane was used for **1,7-i**, it is noteworthy that stable and suitable single crystals of its *1,6* couterpart were only obtained via slow evaporation from toluene. Beyond confirming the structure of each isomer (Fig. 3), X-ray diffraction analyses also revealed, in both cases, regardless of the grafting position, (*i*) relatively twisted PDI backbones with similar dihedral angles (of *ca* 19°) between the two subplanes and (*ii*) high torsion angles (>44°) of the PDI cores with the bulky IDT arms, hindering their aggregation and resulting in a good solubility in common organic solvents (Figs. S20–S24).

The two isomers were analyzed by UV-visible spectroscopy revealing a strong absorption in the visible/near-infrared region in both solution and as thin films (Fig. 4). Optical data are gathered in Table 1.

As expected, similar patterns were recorded showing three maxima at *ca* 320 nm, 460 nm and in the 550–650 nm region assigned to π-π* transitions localized on each building blocks, *ie*, on the IDT and on the PDI units, and to a charge transfer (CT) transition from the electron rich substituents (IDT) to the electro deficient central core (PDI) respectively. Nonetheless, comparison of the spectra clearly highlights the impact of the grafting positions on the electronic properties since all absorption bands of **1,7-i** are significantly red shifted with respect to those of **1,6-i**, particularly in the low energy region (CT band) resulting in a lower optical band gap for **1,7-i** (1.56 eV *vs* 1.66 eV), as determined from the onset of absorption of the thin-films at low energy. This result underlines the enhanced π-electronic delocalization of the *1,7*-regioisomer.

The electrochemical properties of the isomers were characterized by cyclic voltammetry, performed in dichloromethane using NBu_4PF_6 as supporting electrolyte. One reversible reduction wave at the same reduction peak potential ($E_{pc} = -1.05$ V *vs* Fc/Fc^+) was recorded for both regioisomers (Fig. 5).

In the positive potential region, an irreversible oxidation wave was observed at different oxidation peak potentials (E_{pa}) of 0.83 V and 0.89 V for **1,7-i** and **1,6-i** respectively, thus revealing a deeper highest occupied molecular orbital (HOMO) level for **1,6-i** (Table 2). The electrochemical gap determined by the difference of the onset of oxidation and reduction was estimated to 1.89 eV and 1.85 eV for **1,6-i** and **1,7-i** respectively (Table 2) following the same trend observed by spectroscopy (Figs. 4 and S19).

The better conjugation in the *1,7*-substituted derivative and the deeper HOMO level of the *1,6*-regioisomer observed experimentally were afterward investigated from a computational chemistry point of view. Optimized geometries (Fig. S17, Tables S1,S2), orbital density distributions and energies of the frontier molecular levels were simulated by density functional theory (DFT) method using B3LYP model with a 6–311G(d) basis set (Fig. 6).

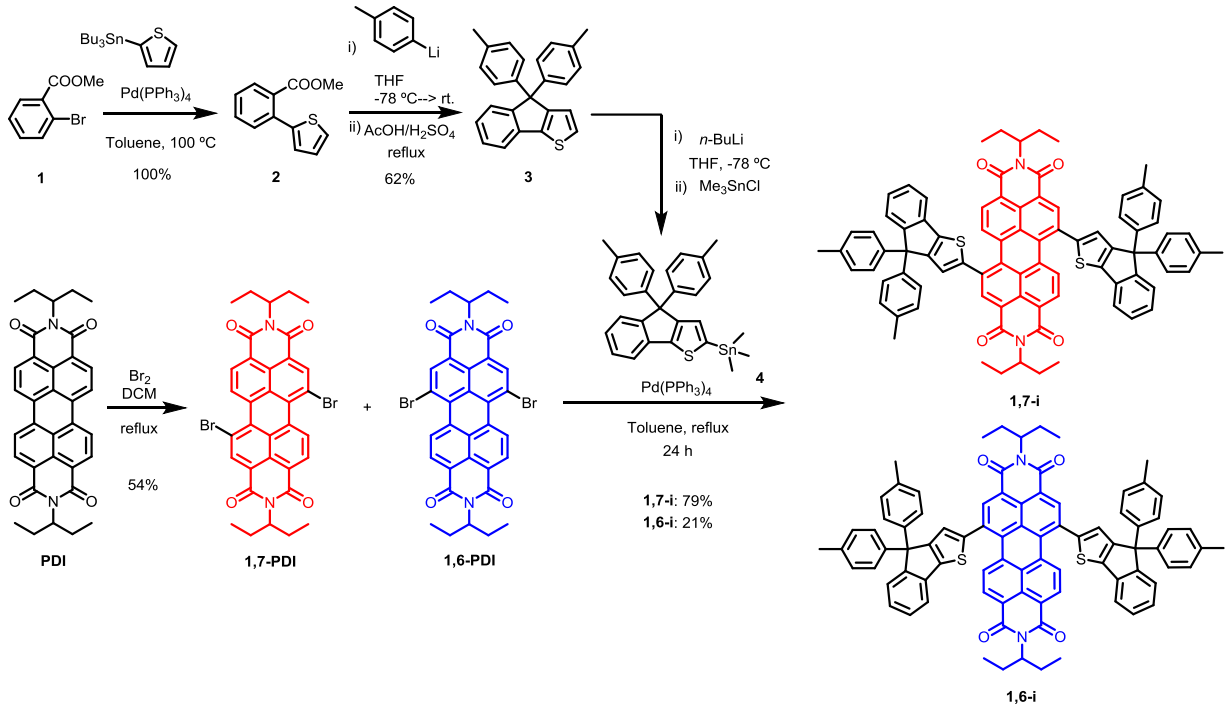

Scheme 1. Synthetic route to **1,6-i** and **1,7-i**.

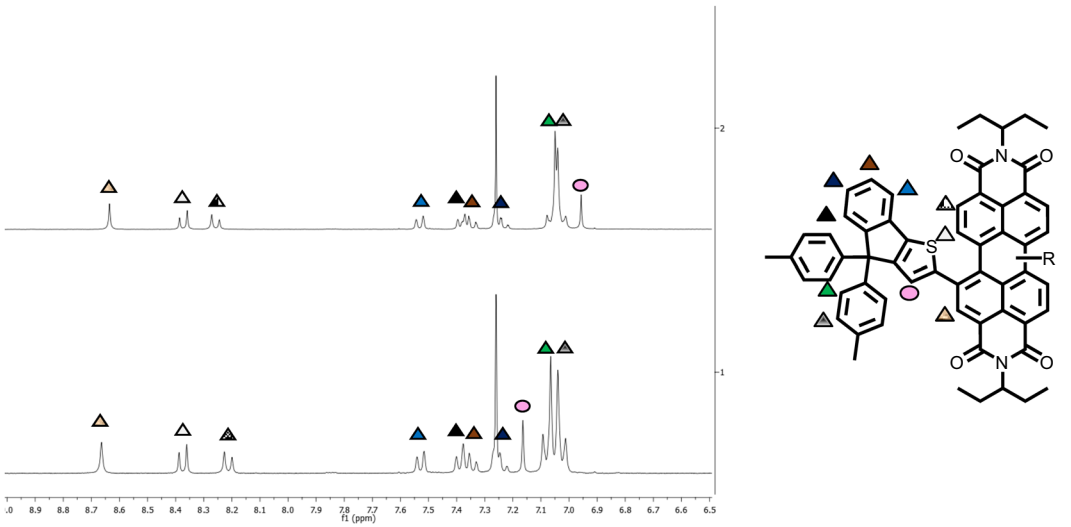

Figure 2. ^{1}H NMR (300 MHz) spectra of **1,6-i** (top) and **1,7-i** (bottom) in $CDCl_3$ at 25 °C.

While LUMO levels are centered on the PDI units, it turns out that the electron densities of the HOMO levels are partially delocalized along the different constituting building blocks. Interestingly, and contrary to **1,6-i**, the HOMO distribution in **1,7-i** appears to be nearly symmetrical and well balanced between the two constituting naphthyl moieties of the PDI core. The charge transfer (CT) character of the lowest energy absorption bands, assigned to HOMO → LUMO transitions, were confirmed by time-dependent DFT (TD-DFT) calculations (Fig. S18 and Table S3). This method also emphasized, through a population analysis, the higher contribution of the IDT arms to the HOMO in **1,7-i** (77% *vs* 71% for **1,6-i**). Hence, with almost similar LUMO levels (88% on the PDI for both isomers), the stronger CT character of **1,7-i** contributes in increasing its HOMO level and therefore reducing its bandgap.

To further investigate the impact of the grafting position of PDI derivatives and more specifically, the impact on their photovoltaic properties, air-processed bulk heterojunction (BHJ) solar cells with inverted architecture (ITO/ZnO/**PTB7-Th**: **1,6-i** or **1,7-i**/MoO_x/Ag) were fabricated. For the sake of comparison, each regioisomer was first blended with the same donor polymer, namely the **PTB7-Th**, in a 1:1 w/w ratio at 10 mg/mL total concentration in chlorobenzene. The resulting devices were tested and the typical density-voltage (J-V) curves recorded

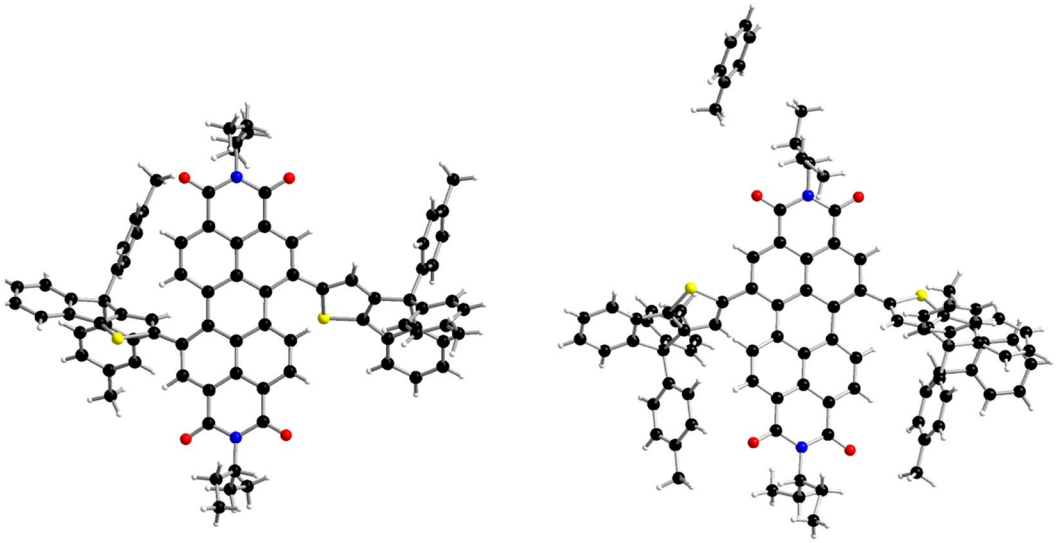

Figure 3. Molecular structures of **1,7-i** (left) and **1,6-i** (right) obtained by X-ray diffraction.

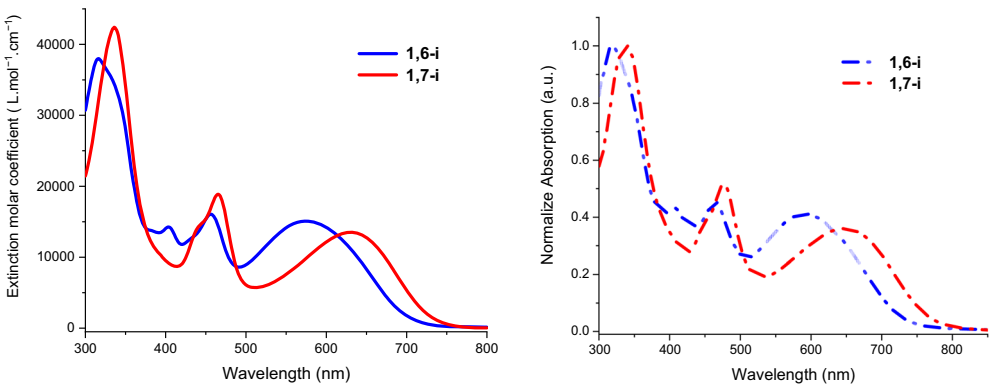

Figure 4. UV-Vis absorption spectra of **1,6-i** (blue line) and **1,7-i** (red line) in CH_2Cl_2 (left) and as thin film on glass (right).

Compound	λ_{max}^{ABS} (nm) in DCM	ε (M^{-1} cm^{-1})	λ_{max}^{ABS} (nm) in film	E_g^{opt} (eV)
1,6-i	573	16000	591	1.66
	456	17000	465	
	316	41000	318	
1,7-i	630	14000	650	1.56
	465	17000	478	
	336	41000	338	

Table 1. Optical data of **1,6-i** and **1,7-i** recorded in dichloromethane solutions (10^{-6} M) and on glass sheets.

under an AM 1.5 simulated solar illumination in air are depicted in Fig. 7 together with the respective EQE spectra.

Devices prepared with **1,6-i** led to better power conversion efficiencies than those of **1,7-i**, mainly due to the higher short circuit current density (J_{sc}) and fill factor (*FF*) parameters (Table 3). While comparable open circuit voltage (V_{oc}) of 0.86 V for **1,6-i** and 0.89 V for **1,7-i** were measured, in agreement with the similar LUMO levels of the regioisomers, **1,6-i** based devices exhibited a *FF* of 41% and a J_{sc} of 4.7 mA cm^{-2} *vs* 33% and 2.4 mA cm^{-2} for **1,7-i**, resulting in PCEs of 1.6% *vs* 0.7% respectively. This two-fold reduction of J_{sc} can also be observed in the external quantum efficiency spectra since the maximum photon-to-electron conversion of **1,7-i** based organic solar cell (OSC) barely exceeded 9% whereas approximatively 18% was reached for **1,6-i** based devices.

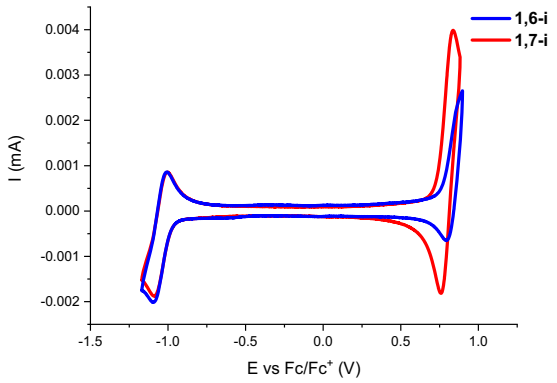

Figure 5. Cyclic voltammograms of **1,7-i** (red) and **1,6-i** (blue) at a concentration of 0.5 mM in 0.10 M Bu_4NPF_6/CH_2Cl_2, 100 mV s^{-1}, Pt working electrode.

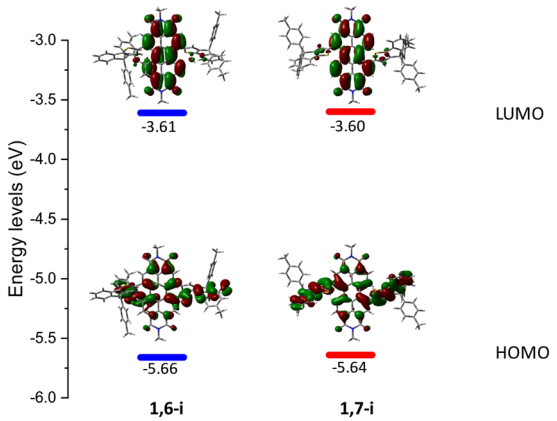

Figure 6. HOMO and LUMO electron density and energy levels calculated by DFT for **1,6-i** and **1,7-i**.

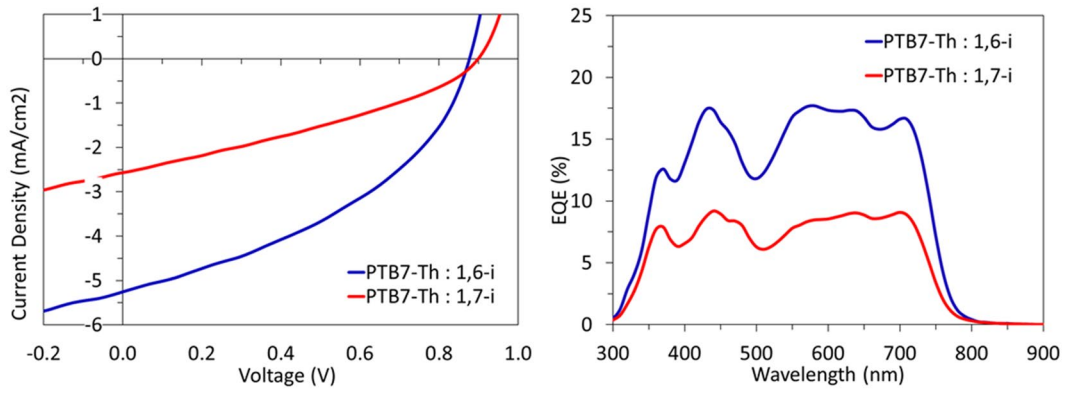

Figure 7. J –V curves (left) and EQE spectra (right) of **1,7-i** (red) and **1,6-i** (blue) based OSCs.

Compound	E_{pa} ($V_{/Fc/Fc+}$)	E_{pc} ($V_{/Fc/Fc+}$)	E_{HOMO}[eV]	E_{LUMO}[eV]	ΔE^{elec} [eV]
1,6-i	0.89	−1.05	−5.64	−3.75	1.89
1,7-i	0.83	−1.05	−5.60	−3.75	1.85

Table 2. Electrochemical data recorded at a concentration of 0.5 mM in 0.10 M Bu_4NPF_6/CH_2Cl_2, 100 mV.s^{-1}, Pt working electrode, Reference: Fc/Fc^+. $E_{HOMO} = -(E_{ox(onset)} + 4.80)$ (eV). $E_{LUMO} = -(E_{red(onset)} + 4.80)$ (eV).

Acceptor	V_{oc} (V)		J_{sc} (mA/cm^2)		*FF* %		PCE %	
1,6-i	0.87	(0.86)	5.3	(4.7)	41	(41)	1.9	(1.6)
1,7-i	0.89	(0.89)	2.6	(2.4)	34	(33)	0.8	(0.7)

Table 3. Organic solar cell device parameters for 1:1 PTB7-Th: **1,7-i** and PTB7-Th: **1,6-i** active layers, obtained from 10 mg/mL solutions in chlorobenzene. Average values in brackets.

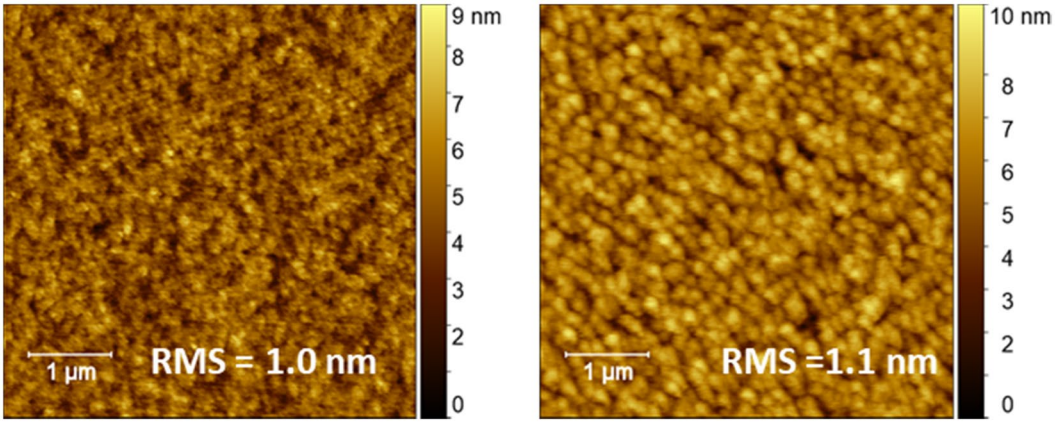

Figure 8. AFM images of **1,6-i** (left) and **1,7-i** (right) based photoactive layers.

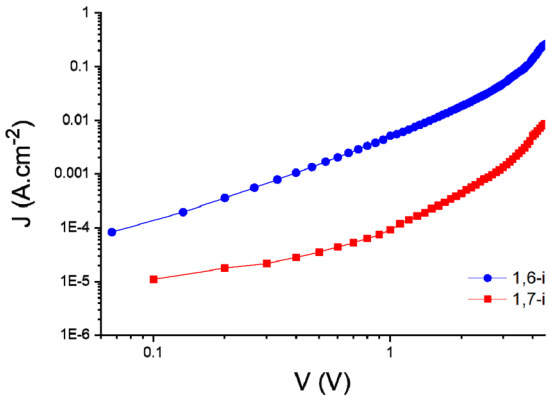

Figure 9. Electron mobility μ_e of **1,6-i** (blue) and **1,7-i** (red) based devices.

The nanoscale topography of the active layers was investigated by atomic force microscopy (AFM). As shown in Fig. 8, both **1,6-i** and **1,7-i** based blends appear similar in roughness, with comparable RMS values of 1.0 and 1.1 nm, respectively.

The slightly more granular nature of the PTB7-Th: **1,7-i** films might be contributing to the lower density of carriers generated (and collected) in the devices, although morphology is hardly the only cause of these low currents and fill factors. Consequently, the electron mobility (μ_e) of each regioisomer was evaluated and compared using the space charge limited current (SCLC) method (Fig. 9).

Electron-only devices (ITO/ZnO/**1,6-i** or **1,7-i**/Al) were thus fabricated revealing a difference of mobility between the two PDI derivatives of *ca* an order of magnitude. While a μ_e of *ca* 7.1×10^{-6} cm^2 V^{-1} s^{-1} was measured for **1,7-i**, the *1,6*-isomer was indeed characterized by an electron mobility of *ca* 8.5×10^{-5} cm^2 V^{-1} s^{-1}, which in consistency with the difference of *Jsc* and *FF*. Consequently, adding an increasing quantity of the *1,7*-isomer to pure **1,6-i** based devices would normally have an impact on their photovoltaic performances, and conversely. Hence, devices made from mixtures of isomers with ratios of 9:1, 7:3, 5:5, 3:7 and 1:9 were finally prepared, characterized and compared to their pure counterparts. As depicted in Fig. 10, increasing the quantity of **1,7-i** results in a significant decrease of both the *Jsc* and *FF* (see Table S5), thus demonstrating that the latter has, in this case, a detrimental effect on the overall performances.

Conclusion

Generated during the dibromination of the PDIs as a minor product and usually considered as an impurity, the *1,6*-dibromo PDI has not attracted much attention, particularly in the field of organic photovoltaics. In addition to the seminal paper reported by Ge *et al.*[34], we demonstrate herein that using the more conjugated *1,7*-isomer

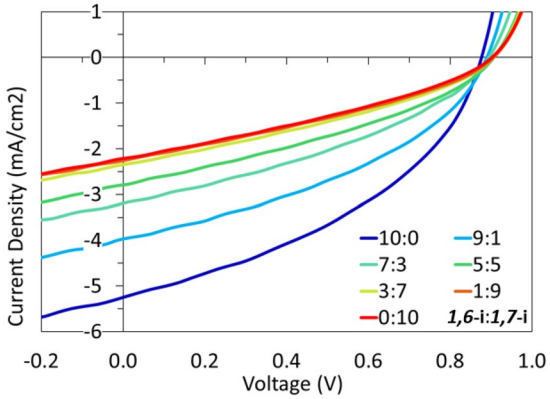

Figure 10. J –V curves of devices prepared with different ratios of **1,6-i** and **1,7-i**.

to prepare new non fullerene acceptors is not an absolute rule to efficiency. In our case, the less conjugated *1,6* derivative indeed led to a two-fold improvement of the power conversion efficiency in comparative devices, which could be slightly enhanced by optimizing the active layer preparation and deposition (PCE up to 1.9%). Moreover, adding an increasing quantity of the *1,7*-isomers to **1,6-i** based devices resulted in a significant decrease of their photovoltaic performances, confirming that the commonly used *1,7*-isomer can be herein considered as a contaminant.

Consequently, this paper highlights the impact of both the grafting position of the PDI and the nature of the end-capping moieties on photovoltaic and charge transport properties and will hopefully contribute in reconsidering conventional design principles and above all, the use of *1,6*-difunctionalized isomer in some organic electronics.

Materials and Methods

General information. All reagents and chemicals from commercial sources were used without further purification unless specified. Solvents were dried and purified using standard techniques. Flash chromatography was performed with analytical-grade solvents using ALDRICH silica gel (technical grade, pore size 60 Å, 230–400 mesh particle size). Flexible plates ALUGRAM Xtra SIL G UV254 from MACHEREY-NAGEL were used for TLC. Compounds were detected by UV irradiation (BIOBLOCK SCIENTIFIC). NMR spectra were recorded with a BRUKER AVANCE III 300 (1H, 300 MHz and 13C, 75 MHz) or a BRUKER AVANCE DRX500 (1H, 500 MHz; 13C, 125 MHz). ^{13}C APT show CH_2 and quaternary as positive while CH and CH_3 as negative. Chemical shifts are given in ppm relative to TMS and coupling constants J in Hz. IR spectra were recorded on a BRUKER spectrometer VERTEX 70 and UV-vis spectra with a PERKIN ELMER 950 spectrometer. Matrix Assisted Laser Desorption/Ionization was performed on MALDI-TOF MS BIFLEX III BRUKER DALTONICS spectrometer using DCTB+ as matrix. High resolution mass spectrometry (HRMS) was performed with a JEOL JMS-700 B/E[38,39].

Cyclic voltammetry was performed using a BIOLOGIC SP-150 potentiostat with positive feedback compensation in 0.10 M Bu_4NPF_6/CH_2Cl_2 (HPLC grade). Experiments were carried out in a one-compartment cell equipped with a platinum working electrode (2 mm of diameter) and a platinum wire counter electrode. A silver wire immersed in 0.10 M Bu_4NPF_6/CH_2Cl_2 was used as pseudo-reference electrode and checked against the ferrocene/ferrocenium couple (Fc/Fc+) before and after each experiment. The potentials were then expressed *vs* Fc/Fc+. X-ray single-crystal diffraction data (Table S4) were collected on an AGILENT SUPERNOVA diffractometer equipped with Atlas CCD detector and micro-focus Cu-K_α radiation. The structures were solved by direct methods and refined on F^2 by full matrix least-squares techniques using SHELX programs (G. M. SHELDRICK 2013–2016). All non-H atoms were refined anisotropically and multiscan empirical absorption was corrected using CRYSALISPRO program (CRYSALISPRO, AGILENT TECHNOLOGIES, 2015–2019). The H atoms were included in the calculation without refinement[40,41].

The identity of new compounds was confirmed by NMR, IR and high-resolution MALDI-TOF mass spectroscopy (Figs. S1–S16). The synthesis of **(4,4-di-*p*-tolyl-4*H*-indeno[1,2-*b*]thiophen-2-yl)trimethylstannane (4)** was adapted from a preparation reported in the literature[42]. Both **1,6-i** and **1,7-i** isomers were prepared according to a preparation published by Rybtchinski & *al.*[37].

Synthesis. *Methyl 2-(thiophen-2-yl)benzoate (2).* Degassed toluene (30 mL) was added to a mixture of methyl-2-bromobenzoate **1** (5 g, 22.79 mmol) and tributyl(thiophen-2-yl)stannane (10.2 g, 27.34 mmol). $Pd(PPh_3)_4$ (526 mg, 0.46 mmol) was further added before refluxing the reaction mixture for 24 h. The latter was then cooled to room temperature and the solvent removed under *vacuum*. Purification of the crude was performed by column chromatography on silica gel (eluent: petroleum ether/dichloromethane, 1:3) affording 4.97 g of a colourless oil (quantitative). **^{1}H-NMR** (300 MHz, $CDCl_3$): δ 7.73 (dt, $J = 7.6$ Hz, 1.1 Hz, 1H), 7.51–7.47 (m, 2H), 7.40 (ddd, $J = 8.8$ Hz, 7.8 Hz, 4.2 Hz, 1H), 7.35 (dd, $J = 4.9$ Hz, 1.4 Hz, 1H), 7.09–7.02 (m, 2H), 3.78 (s, 3H).

4,4-di-p-tolyl-4H-indeno[1,2-b]thiophene (3). To a solution of 4-bromotoluene (9.4 g, 54.98 mmol) in distilled THF (40 mL) was added dropwise *n*-BuLi (2.5 M in hexane, 22 mL, 54.98 mmol) at −78 °C. After 1 h, a diluted solution of **2** (4.8 g, 22 mmol) in dry THF (40 mL) was slowly added at −78 °C. The mixture was then stirred

for 16 h at room temperature before being poured in water (125 mL). The aqueous layer was extracted with dichloromethane (200 mL × 2), the organic phase was dry over $MgSO_4$ and the solvent removed under reduced pressure. The resulting crude was thereafter suspended in a mixture of glacial acetic acid (125 mL) and H_2SO_4 (2 mL). After 3 h of reflux, the reaction was cooled to room temperature and the precipitated filtrated and washed with water, ethanol and petroleum ether. Once dried, 4.8 g of a white powder were recovered (62%). **^{1}H-NMR** (300 MHz, $CDCl_3$): δ 7.45 (d, $J = 7.5$ Hz, 1H), 7.35 (d, $J = 7.6$ Hz, 1H), 7.32–7.26 (m, 2H), 7.16 (dt, $J = 7.5$ Hz, 1.1 Hz, 1H), 7.10 (d, $J = 8.1$ Hz, 4H), 7.05–6.99 (m, 1H), 2.29 (s, 6H).

(4,4-di-p-tolyl-4H-indeno[1,2-b]thiophen-2-yl)trimethylstannane (4). **3** (2 g, 5.67 mmol) was dissolved in distilled THF (20 mL) under argon, then *n*-BuLi (2.5 M in hexane, 2.2 mL, 7.94 mmol) was added dropwise at −78 °C and the reaction was stirred for 1 h 30 min. Trimethyl tin chloride (1 M in hexane, 8.5 mL, 8.51 mmol) was then added before warming the reaction mixture to room temperature. The overnight stirred solution was quenched with water and extracted with AcOEt. The organic layer was washed with KF solution (sat.) and water, dry over Mg_2SO_4 and the solvent evaporated under *vacuum*. The resulting crude was used without further purification. **^{1}H-NMR** (300 MHz, $CDCl_3$): δ 7.43 (d, $J = 7.4$ Hz, 1H), 7.32 (d, $J = 7.6$ Hz, 1H), 7.26 (td, $J = 7.6$ Hz, J = 1,1 Hz, 1H), 7.17–7.07 (m, 5H), 7.08–6.99 (m, 5H), 2.29 (s, 6H), 0.36 (s, 9H).**^{13}C-NMR** (75 MHz, $CDCl_3$): δ 157.6, 153.9, 147.1, 142.2, 141.9, 137.3, 136.2, 130.4, 130.0, 127.9, 127.8, 127.3, 126.4, 125.4, 119.5, 62.3, 21.0. **MS** (MALDI-dit+) m/z: 516.0 [M+].

Synthesis of 1,6-i and 1,7-i. To a blend of halogenated perylene diimide (**1,7-** and **1,6-PDI**) (150 mg, 0.25 mmol) were added **4** (317 mg, 0.62 mmol), $Pd(PPh_3)_4$ (25 mg, 0.02 mmol) and 10 ml of dry toluene. The reaction mixture was then stirred and refluxed for 24 h under inert conditions. Once concentrated under *vacuum*, the crude was purified by column chromatography (eluent: dichloromethane/petroleum ether) affording **(1,6-i)** and **(1,7-i)** in 21% and 79% yield respectively. **(1,6-i)**. **^{1}H-NMR** (300 MHz, $CDCl_3$): δ 8.64 (s, 2H), 8.38 (d, $J = 8.1$ Hz, 2H), 8.26 (d, $J =$ 8.2 Hz, 2H), 7.53 (d, $J = 7.6$ Hz, 2H), 7.42–7.32 (m, 4H), 7.24 (td, $J = 7.6$, 1.2 Hz, 2H), 7.10–7.00 (m, 16H), 6.96 (s, 2H), 5.16–4.97 (m, 2H), 2.42–1.78 (m, 20H), 0.94 (t, $J = 7.6$ Hz, 12H).**^{13}C-NMR** (75 MHz, $CDCl_3$): δ 157.5, 153.5, 146.5, 143.5, 141.3, 136.9, 136.8, 134.9, 134.0, 129.6, 129.4, 129.2, 129.0, 128.9, 128.0, 127.9, 127.8, 126.6, 126.4, 123.1, 122.4, 120.0, 63.5, 57.9, 57.7, 25.2, 25.1, 21.1, 11.6, 11.4. **IR** (neat): $\nu = 3090–3015\ cm^{-1}$ (C_{sp2}-H, Ar), 2965–2862 cm^{-1} (C_{sp3}-H), 1699 cm^{-1} (C=O), 1653 cm^{-1} (C=O), 1580–1458 cm^{-1} (C=C, Ar), 1336 cm^{-1} (C_{sp3}-N), 1321 cm^{-1} (C_{sp3}-N). **UV-Vis** (CH_2Cl_2): λ_{max} (ε) = 573 nm (16000 L.mol^{-1}.cm^{-1}), 456 nm (17000 L.mol^{-1}.cm^{-1}), 316 nm (41000 L.mol^{-1}.cm^{-1}). **MS** (MALDI-dctb+) m/z: 1230.6 [M+]. **HRMS** (FAB+): calculated for $C_{84}H_{66}N_2O_4S_2$ 1230.4458, found 1230.4446. **(1,7-i)** was obtained in the second fraction as a green solid. (240 mg, 79%). **^{1}H-NMR** (300 MHz, $CDCl_3$): δ 8.67 (s, 2H), 8.38 (d, $J = 8.2$ Hz, 2H), 8.22 (d, $J = 8.2$ Hz, 2H), 7.53 (d, $J = 7.3$ Hz, 2H), 7.42–7.32 (m, 4H), 7.25 (td, $J = 7.5$, 1.1 Hz, 2H), 7.17 (s, 2H), 7.08 (d, $J = 8.5$ Hz, 8H), 7.03 (d, $J = 8.2$ Hz, 8H), 5.11–5.00 (m, 2H), 2.35–2.18 (m, 16H), 2.00–1.84 (m, 4H), 0.91 (t, $J = 7.5$ Hz, 12H).**^{13}C-NMR** (75 MHz, $CDCl_3$): δ 157.7, 153.5, 146.3, 143.8, 141.3, 136.8, 136.8, 135.0, 133.8, 129.8, 129.5, 129.2, 128.4, 127.9, 127.8, 126.7, 126.5,123.8, 120.1, 63.5, 57.8, 25.2, 21.1, 11.5. **IR** (neat): $\nu = 3056–3018\ cm^{-1}$ (C_{sp2}-H, Ar), 2962–2876 cm^{-1} (C_{sp3}-H), 1696 cm^{-1} (C=O), 1654 cm^{-1} (C=O), 1594–1506 cm^{-1} (C=C, Ar), 1324 cm^{-1} (C_{sp3}-N). **UV-Vis** (CH_2Cl_2): λ_{max} (ε) = 630 nm (14000 L.mol^{-1}.cm^{-1}), 465 nm (17000 L.mol^{-1}.cm^{-1}), 336 nm (41000 L.mol^{-1}.cm^{-1}). **MS** (MALDI-dctb+) m/z: 1230.6 [M+]. **HRMS** (FAB+): calculated for $C_{84}H_{66}N_2O_4S_2$ 1230.4458, found 1230.4434.

Computational calculation methodology. Ground-state density-functional theory (DFT) geometry optimizations and time-dependent density-functional theory (TD-DFT) calculations were carried out using GAUSSIAN 16[43] suite package. B3LYP/6–311G* basis sets were chosen for all the atomic species. In order to take into account solvation effects in the reproduction of the absorption spectra, solvent dichloromethane molecules were treated as a polarizable continuum (PCM).

Organic photovoltaic devices fabrication and characterization. PTB7-Th: **1,6-i** or **1,7-i** solutions were prepared in air, from 10 mg/mL solutions of the single components, which were stirred for approximatively 2 hours before mixing in the required proportions. The final solutions were stirred for at least 1 hour before deposition on substrates. ZnO precursor solutions were prepared following the sol-gel method proposed by Sun *et al.*[44], 1.0 g of zinc acetate dihydrate, 0.280 mL of ethanolamine and 10.0 mL of 2-methoxy ethanol were mixed in air and stirred overnight at room temperature before use. All studied films were prepared as follow: ITO-coated glass substrates were first cleaned by surfactant/water scrubbing, followed by sequentially ultra-sonicating in de-ionized water, acetone and isopropanol (10+ minutes each) before use. ITO substrates were then dried with pressurized air and UV-Ozone treated for 30 minutes. A ZnO precursor solution was spin-coated onto the ITO substrate at a speed of 4200 rpm for 55 s and then thermally annealed at 200 °C in air for 20 min. The organic layer was then spin-coated at room temperature, in air at 1000 rpm for 50 s. Solar cells were fabricated following the initial procedure for cleaning, ZnO deposition and organic layer deposition reported above. The fabricated films were then moved to an N_2 atmosphere glovebox and left overnight before evaporating the top electrodes consisting of 10 nm of MoO_x (electron transport interlayer) followed by 100 nm of Ag (anode), which were thermally deposited under high vacuum (10^{-5} mbar). Current density-voltage (J-V) characteristics were measured using a Keithley 2420 Source Measure Unit. Solar cell performance used an Air Mass 1.5 Global (AM 1.5G) Solar Simulator (Newport, Model 92251A-1000) with an irradiation intensity of 100 mWcm-2, which was measured by a calibrated silicon solar cell and a readout meter (Newport, Model 91150V).

Atomic force microscopy (AFM). AFM measurements were performed by using a TT-2 AFM (AFM Workshop, USA) in the tapping mode and WSxM software with a 0.01–0.025 Ohm/cm Sb (n) doped Si probe with a reflective back side aluminium coating.

SCLC measurements. A solution of neat isomers, namely **1,6-i** or **1,7-i** (20 mg/mL) in chloroform was spun-cast at 1000 rpm on the above described ZnO coated substrates to provide organic layers of *ca*. 140 nm and 180 nm respectively. Calcium (7 nm) and aluminium (100 nm) were thermally evaporated under a *vacuum* of 1.5×10^{-5} Torr, through a shadow mask defining active areas of 12.60 mm^2, 3.10 mm^2 and 0.78 mm^2 per substrate. Electron mobilities μ_e were evaluated using the Mott-Gurney law, ie, $JSCLC = (9/8)\varepsilon_0\varepsilon_r\mu_e(V^2/d^3)$ where εr is the static dielectric constant of the medium ($\varepsilon_r = 3$) and d, the thickness of the active layer.

Received: 3 December 2019; Accepted: 3 February 2020;
Published online: 24 February 2020

References

1. Wadsworth, A. *et al*. Critical review of the molecular design progress in non-fullerene electron acceptors towards commercially viable organic solar cells. *Chem. Soc. Rev.* **48**, 1596–1625 (2019).
2. Sun, H., Chen, F. & Chen, Z. K. Recent progress on non-fullerene acceptors for organic photovoltaics. *Mater. Today* **24**, 94–118 (2019).
3. Zhang, G. *et al*. Nonfullerene Acceptor Molecules for Bulk Heterojunction Organic Solar Cells. *Chem. Rev.* **118**, 3447–3507 (2018).
4. Josse, P. *et al*. Phthalimide end-capped thienoisoindigo and diketopyrrolopyrrole as non-fullerene molecular acceptors for organic solar cells. *J. Mater. Chem. A* **4**, 250–256 (2015).
5. Yan, C. *et al*. Non-fullerene acceptors for organic solar cells. *Nat. Rev. Mater.* **3**, 1–8 (2018).
6. Yuan, J. et al. Single-Junction Organic Solar Cell with over 15% Efficiency Using Fused-Ring Acceptor with Electron-Deficient Core. *Joule* 1–12, https://doi.org/10.1016/j.joule.2019.01.004 (2019).
7. Cui, Y. *et al*. Over 16% efficiency organic photovoltaic cells enabled by a chlorinated acceptor with increased open-circuit voltages. *Nat. Commun.* **10**, 2515–2522 (2019).
8. Meng, L. *et al*. Organic and solution-processed tandem solar cells with 17.3% efficiency. *Science* **361**, 1094–1098 (2018).
9. Huang, C., Barlow, S. & Marder, S. R. Perylene-3,4,9,10-tetracarboxylic Acid Diimides: Synthesis, Physical Properties, and Use in Organic Electronics. *J. Org. Chem.* **76**, 2386–2407 (2011).
10. Zhan, X. *et al*. Rylene and Related Diimides for Organic Electronics. *Adv. Mater.* **23**, 268–284 (2011).
11. Singh, R. *et al*. Fullerene-free organic solar cells with an efficiency of 3.7% based on a low-cost geometrically planar perylene diimide monomer. *J. Mater. Chem. A* **2**, 14348–14353 (2014).
12. Singh, R. *et al*. Unraveling the efficiency-limiting morphological issues of the perylene diimide-based non-fullerene organic solar cells. *Sci. Rep.* **8**, 2849–2857 (2018).
13. Lee, J. *et al*. A Nonfullerene Small Molecule Acceptor with 3D Interlocking Geometry Enabling Efficient Organic Solar Cells. *Adv. Mater.* **28**, 69–76 (2016).
14. Ye, T., Singh, R., Butt, H.-J., Floudas, G. & Keivanidis, P. E. Effect of Local and Global Structural Order on the Performance of Perylene Diimide Excimeric Solar Cells. *ACS Appl. Mater. Interfaces* **5**, 11844–11857 (2013).
15. Cliķeman, T. T. *et al*. Core Perylene Diimide Designs via Direct Bay- and ortho-(Poly)trifluoromethylation: Synthesis, Isolation, X-ray Structures, Optical and Electronic Properties. *European J. Org. Chem.* **2015**, 6641–6654 (2015).
16. Handa, N. V., Mendoza, K. D. & Shirtcliff, L. D. Syntheses and Properties of 1,6 and 1,7 Perylene Diimides and Tetracarboxylic Dianhydrides. *Org. Lett.* **13**, 4724–4727 (2011).
17. Shaw, S. A. *et al*. Synthesis of Biologically Active Piperidine Metabolites of Clopidogrel: Determination of Structure and Analyte Development. *J. Org. Chem.* **80**, 196–203 (2015).
18. Zhang, X. *et al*. Cooperatively tuning phase size and absorption of near IR photons in P3HT:Perylene diimide solar cells by bay-modifications on the acceptor. *J. Phys. Chem. C* **118**, 24212–24220 (2014).
19. Wang, J. & Zhan, X. Rylene Diimide Electron Acceptors for Organic Solar Cells. *Trends Chem*. https://doi.org/10.1016/j.trechm.2019.05.002 (2019).
20. Wang, H. *et al*. Perylene diimide based star-shaped small molecular acceptors for high efficiency organic solar cells. *J. Mater. Chem. C* **7**, 819–825 (2019).
21. Wang, J., Peng, J., Liu, X. & Liang, Z. Efficient and Stable Ternary Organic Solar Cells Based on Two Planar Nonfullerene Acceptors with Tunable Crystallinity and Phase Miscibility. *ACS Appl. Mater. Interfaces* **9**, 20704–20710 (2017).
22. Ganesamoorthy, R., Vijayaraghavan, R., Ramki, K. & Sakthivel, P. Synthesis, characterization of bay-substituted perylene diimide based D-A-D type small molecules and their applications as a non-fullerene electron acceptor in polymer solar cells. *J. Sci. Adv. Mater. Devices* **3**, 99–106 (2018).
23. Wu, J. *et al*. Effects of conjugated bridges on the photovoltaic properties of ortho-functionalized perylene diimides for non-fullerene polymer solar cells. *J. Mater. Chem. C* **6**, 13171–13178 (2018).
24. Abd-Ellah, M. *et al*. Interfacial ZnO Modification Using a Carboxylic Acid Functionalized N-Annulated Perylene Diimide for Inverted Type Organic Photovoltaics. ACS Appl. Electron. *Mater.* **1**, 1590–1596 (2019).
25. Wu, M. *et al*. Novel Star-Shaped Helical Perylene Diimide Electron Acceptors for Efficient Additive-Free Nonfullerene Organic Solar Cells. *ACS Appl. Mater. Interfaces* **10**, 27894–27901 (2018).
26. McAfee, S. M. *et al*. Simply Complex: The Efficient Synthesis of an Intricate Molecular Acceptor for High-Performance Air-Processed and Air-Tested Fullerene-Free Organic Solar Cells. *Chem. Mater.* **29**, 1309–1314 (2017).
27. Dayneko, S. V., Hendsbee, A. D., Cann, J. R., Cabanetos, C. & Welch, G. C. Ternary organic solar cells: using molecular donor or acceptor third components to increase open circuit voltage. *New J. Chem.* **43**, 10442–10448 (2019).
28. Payne, A.-J. *et al*. Donor or Acceptor? How Selection of the Rylene Imide End Cap Impacts the Polarity of π-Conjugated Molecules for Organic Electronics. *ACS Appl. Energy Mater.* **1**, 4906–4916 (2018).
29. Handa, N. V., Shirtcliff, L. D., Lavine, B. K., Powell, D. R. & Berlin, D. K. 1,6-and 1,7-regioisomers of perylene tetracarboxylic dianhydride and diimide: The effects of neutral bay substituents on the electrochemical and structural properties. *Phosphorus, Sulfur Silicon Relat. Elem.* **189**, 738–752 (2014).
30. Würthner, F. *et al*. Preparation and Characterization of Regioisomerically Pure 1,7-Disubstituted Perylene Bisimide Dyes. *J. Org. Chem.* **69**, 7933–7939 (2004).
31. Dey, S., Efimov, A. & Lemmetyinen, H. Diaryl-substituted perylene bis(imides): Synthesis, separation, characterization and comparison of electrochemical and optical properties of 1,7-and 1,6-regioisomer. *European J. Org. Chem.* **12**, 2367–2374 (2012).
32. Kozma, E. *et al*. A joint experimental and theoretical study on the electro-optical properties of 1,6- and 1,7-fluorenyl disubstituted perylene diimide isomers. *New J. Chem.* **42**, 1061–1066 (2018).
33. Zhang, X., Zhan, C., Zhang, X. & Yao, J. Orientation of bromination in bay-region of perylene diimides. *Tetrahedron* **69**, 8155–8160 (2013).
34. Liu, Y. *et al*. Perylenebisimide regioisomers: Effect of substituent position on their spectroscopic, electrochemical, and photovoltaic properties. *Dye. Pigment.* **121**, 363–371 (2015).
35. Mao, Y. *et al*. Molecular Ordering and Performance of Ternary Nonfullerene Organic Solar Cells via Bar-Coating in Air with an Efficiency over 13%. *ACS Appl. Mater. Interfaces* **11**, 35827–35834 (2019).

36. Cheng, P., Li, G., Zhan, X. & Yang, Y. Next-generation organic photovoltaics based on non-fullerene acceptors. *Nat. Photonics* **12**, 131–142 (2018).
37. Rajasingh, P., Cohen, R., Shirman, E., Shimon, L. J. W. & Rybtchinski, B. Selective Bromination of Perylene Diimides under Mild Conditions. *J. Org. Chem.* **72**, 5973–5979 (2007).
38. Labrunie, A., Habibi, A. H., Dabos-Seignon, S., Blanchard, P. & Cabanetos, C. Exploration of the structure-property relationship of push-pull based dyads for single-molecule organic solar cells. *Dye. Pigment.* **170**, 107632 (2019).
39. Labrunie, A. *et al*. Triphenylamine-Based Push-Pull σ-C60Dyad As Photoactive Molecular Material for Single-Component Organic Solar Cells: Synthesis, Characterizations, and Photophysical Properties. *Chem. Mater.* **30**, 3474–3485 (2018).
40. Malacrida, C. *et al*. Impact of the Replacement of a Triphenylamine by a Diphenylmethylamine Unit on the Electrochemical Behavior of Pentaerythritol-Based Push-Pull Tetramers. *Chem. Electro. Chem.* **6**, 4215–4228 (2019).
41. Andrés Castán, J. M. *et al*. Nitration of benzothioxanthene: towards a new class of dyes with versatile photophysical properties. *New J. Chem.* **44**, 900 (2020).
42. Pouchain, L. *et al*. Quaterthiophenes with Terminal Indeno 1,2-b thiophene Units as p-Type Organic Semiconductors. *J. Org. Chem.* **74**, 1054–1064 (2009).
43. Frisch, M. J. et al. Gaussian 16 Gaussian, Inc.: Wallingford CT. (2016).
44. Sun, Y., Seo, J. H., Takacs, C. J., Seifter, J. & Heeger, A. J. Inverted polymer solar cells integrated with a low-temperature-annealed sol-gel-derived ZnO film as an electron transport layer. *Adv. Mater.* **23**, 1679–1683 (2011).

Acknowledgements

Authors thank the MATRIX SFR of the University of Angers. P.S.M. and J.M.A.C. thanks the European Union's Horizon 2020 research and innovation program under Marie Sklodowska Curie Grant agreement No. 722651 (SEPOMO). The region *Pays de la Loire* is also thanked for the "*Etoiles Montantes*" grant (SAMOA project). Finally, GCW and FT acknowledge the University of Calgary and the Canada Foundation for Innovation.

Author contributions

P.S.M. conceived the idea and synthesized/characterized the molecules with the help of J.M.A.C., P.J. and C.D. Devices were fabricated and characterized by F.T. X-ray analysis were performed by M.A., G.W., P.B. and C.C. supervised the troops and edited the manuscript. All authors reviewed the manuscript.

Competing interests

The authors declare no competing interests.

Additional information

Supplementary information is available for this paper at https://doi.org/10.1038/s41598-020-60012-7.

Correspondence and requests for materials should be addressed to G.W., P.B. or C.C.

Reprints and permissions information is available at www.nature.com/reprints.

Publisher's note Springer Nature remains neutral with regard to jurisdictional claims in published maps and institutional affiliations.

Open Access This article is licensed under a Creative Commons Attribution 4.0 International License, which permits use, sharing, adaptation, distribution and reproduction in any medium or format, as long as you give appropriate credit to the original author(s) and the source, provide a link to the Creative Commons license, and indicate if changes were made. The images or other third party material in this article are included in the article's Creative Commons license, unless indicated otherwise in a credit line to the material. If material is not included in the article's Creative Commons license and your intended use is not permitted by statutory regulation or exceeds the permitted use, you will need to obtain permission directly from the copyright holder. To view a copy of this license, visit http://creativecommons.org/licenses/by/4.0/.

© The Author(s) 2020